1 **Role of ammonia on fine-particle pH in agricultural regions of China:**

2 **Comparison between urban and rural sites**

3 Shenbo Wang [a], Lingling Wang [b], Yuqing Li [c], Chen Wang [a], Weisi Wang [b], Shasha Yin [a,

4 *], Ruiqin Zhang [a, *]

5 [a] *Research Institute of Environmental Science, College of Chemistry, Zhengzhou*

6 *University, Zhengzhou, 450001, China*

7 [b] *Department of Environmental Protection of Henan Province, Zhengzhou, 450001,*

8 *China*

9 [c] *Department of Environment Science and Engineering, Tsinghua University, Beijing*

10 *100084, China*

11

12 * Corresponding authors：Shasha Yin and Ruiqin Zhang

13 E-mail addresses: shashayin@zzu.edu.cn；rqzhang@zzu.edu.cn

14

15

16

17

18

19

20

21

Abstract: Particle acidity is a fundamental property that affects atmospheric particulate chemistry. Synchronous online monitoring was performed in two urban sites (e.g., Zhengzhou (U-ZZ) and Anyang (U-AY)) and three rural sites (e.g., Anyang (R-AY), Xinxiang (R-XX), and Puyang (R-PY)) in Henan Province during a haze episode to investigate the pH value and its driving factors in the agricultural regions of China. The pH values of particles calculated by ISORROPIA-II model at rural sites were slightly higher than those at urban sites, with the median (min–max) values of 5.2 (4.8–6.9, R-PY), 5.1 (4.7–6.5, R-AY), 4.9 (4.1–6.8, R-XX), 4.8 (3.9–5.9, U-AY), and 4.5 (3.8–5.2, U-ZZ). Sensitivity tests show that TNH_x (total ammonium (gas + aerosol)), followed by total sulfate, were the important factors that influenced the predicted pH. Generally, particle pH increased with the cation increasing and the decrease in the anion, temperature, and relative humidity. Similar pH values (~3.0) at the required NH_x concentrations for the five sites indicated that the presence of excess NH_x was likely important for the less acidic of $PM_{2.5}$ during the severe haze episodes in this region. Moreover, the concentrations of excess NH_x may drive the higher pH values at rural sites, because of the higher excess NH_x concentrations at rural sites than those at urban sites. The underlying influence of regional transport on local particle pH cannot be neglected by differing the chemical components of $PM_{2.5}$ and meteorological conditions. Air masses transported from rural and agricultural regions may enhance the particle pH value in urban aerosols given the high pH of particles and high ammonia levels. These results suggest that ammonia is urgently needed to be involved in the regional strategy for the improvement of air quality in China.

Keywords: ISORROPIA-II model, Particle acidity, Ammonia, Sensitivity test, Regional transport.

1 Introduction

High concentrations of acids and bases contained in the aqueous phase define the acidity of aerosols (Spurny, 1990). Particle acidity or pH value is an important parameter for atmospheric particulate chemistry, such as the gas-particle portioning of semi-volatile and volatile species (e.g., $NH_{3(g)}/NH_{4(aq)}^+$, $HCl_{(g)}/Cl_{(aq)}^-$, and $HNO_{3(g)}/NO_{3(aq)}^-$), the formation of secondary inorganic and organic aerosols, and the dissolution of metallic elements (Bougiatioti et al., 2016; Meskhidze et al., 2003; Seinfeld and Pandis, 2006; Shi et al., 2019; Shi et al., 2010; Surratt et al., 2010; Wang et al., 2018b). Particle acidity can affect the ecosystem through its influence on wet/dry deposition, atmospheric visibility, and radiative balance (Boucher and Anderson, 1995; Larssen et al., 2006; Pye et al., 2019; Watson, 2002). In addition, high particle acidity has an adverse impact on public health, especially for the cardiopulmonary and respiration system of humans (Dockery et al., 1996; Ostro et al., 1991).

Direct measurements on particle pH are challenging because of the small size and nonideality of chemical species in solvated aerosols. Therefore, thermodynamic models, such as E-AIM (http://www.aim.env.uea.ac.uk/aim/aim.php) and ISORROPIA-II (http://isorropia.eas.gatech.edu) (Clegg et al., 1998; Nenes et al., 1998), which rely on the measurements of particulate and gaseous species, are widely used in estimating particle pH. Generally, the global distribution of fine particulate matter (PM$_{2.5}$, aerodynamic diameter $\leq$ 2.5 μm) pH is bimodal with a population of particles having a mean pH of 1–3 and another population having an average pH closer to 4–5 (Pye et al., 2019). Table 1 shows that PM$_{2.5}$ in mainland China were moderately acidic with pH values that ranged from 3.4–5.7 (Ding et al., 2019; Guo et al., 2017; Liu et al., 2017; Shi et al., 2017, 2019; Song et al., 2018; Wang et al., 2019a), which were 3–5 units higher than those reported in other regions, such as Hong Kong,

63 Singapore, USA, and Greece (Behera et al., 2013; Bougiatioti et al., 2016; Guo et al., 2016; Guo et al.,

64 2014; Pathak et al., 2004).

65 High atmospheric ammonia (TNH_x, gas NH_3 plus particle NH_4^+) is a dominant factor that drives

66 the high $PM_{2.5}$ pH in megacities of China because it suppresses the production of particle hydronium

67 (Cheng et al., 2016; Wang et al., 2016). Liu et al. (2017) argued that excess NH_3 and elevated aerosol

68 water content (AWC) were responsible for the high pH in Beijing. Nevertheless, Guo et al. (2017) and

69 Song et al. (2018) demonstrated that high levels of ammonia did not increase the $PM_{2.5}$ pH into a fully

70 neutralized condition in Beijing and Xi'an, China. Weber et al. (2016) calculated that only large

71 increases in NH_3 together with sulfate reductions can lead to an increase in pH. Correspondingly,

72 higher pH by about 1 unit than urban aerosols was observed in locations of intensive agriculture with

73 high NH_3 concentrations in the southeastern US (Nah et al., 2018). The primary sources for ammonia

74 include agricultural emissions, such as livestock waste, N-fertilizer application, and biomass burning,

75 as well as traffic and industrial emissions (Huang et al., 2012; Shen et al., 2011; Wang et al., 2018a).

76 Field studies have reported that elevated NH_3 and NH_4^+ concentrations were recorded at rural sites in

77 the North China Plain (Meng et al., 2011; Meng et al., 2017; Shen et al., 2011; Wen et al., 2015).

78 Therefore, studying in an agriculturally developed region is needed to obtain insight into the role of

79 ammonia in particle pH. Unfortunately, previous studies mainly concentrated on calculating the

80 particle pH in the megacity of China, and few studies focused on the agricultural regions of China. In

81 addition to ammonia, particle pH can also be influenced by other chemical compositions and

82 meteorological conditions, such as sulfate, AWC, temperature (T), and relative humidity (RH). Sulfate

83 is often the main acid component of aerosols, and largely determines the acidity of $PM_{2.5}$ (Weber et al.,

84   2016). Sensitivity tests in Beijing suggested that sulfate, TNH_x, and T were the common driving factors,

85   and Ca^{2+} and RH were the unique factors in special seasons (Ding et al., 2019). The pH sensitivity

86   based on the 10-year record in Canada showed that chemical compositions had various effects on

87   particle pH under different meteorological conditions; moreover, careful examination for any

88   particular region is needed (Tao and Murphy, 2019).

89   Henan Province is situated in Central China; it has a dense rural population and is a top-ranking

90   province in China in terms of agricultural production and chemical fertilizer consumption (NBS, 2016).

91   NH_3 emission inventory for Henan Province reported that approximately 1031.6 Gg NH_3 was released

92   in Henan in 2015, thereby contributing to approximately 10 % of China's total emissions

93   (approximately 10 Tg) (Huang et al., 2012; Wang et al., 2018a). Livestock waste and N-fertilizer

94   application were major sources for ammonia emissions, which may increase TNH_x concentrations at

95   rural sites than in urban sites. Furthermore, Henan Province is a severely $PM_{2.5}$-polluted region in

96   China. In January 2018, a large-scale and long-lasting haze episode that caused $PM_{2.5}$ concentration to

97   reach 400 μg/m^3 occurred in this region (Wang et al., 2019c). An experiment was performed in two

98   urban and three rural sites in Henan Province to investigate the particle acidity and its driving factor.

99   ISORROPIA-II model was utilized to estimate $PM_{2.5}$ pH using a high-time-resolution dataset. The

100   novelty of the work addressed in the present study is that this study is the first on $PM_{2.5}$ acidity by

101   comparing urban and rural sites in the agricultural regions of China. The specific objectives of the

102   study were presented as follows: (1) Estimation and comparison of the $PM_{2.5}$ pH at the five monitoring

103   sites, (2) identification of the factors that determine the pH, and (3) discussion of the role of ammonia

104   on pH. Our results are helpful to understand the factors that determine particle acidity better.

2 Experiment and methods

2.1 Site descriptions

Field sampling was synchronously conducted from January 12 to 24, 2018 at five sites (i.e., two urban sites located in the center of Zhengzhou (U-ZZ) and Anyang (U-AY), and three sites located in the rural areas of Anyang (R-AY), Xinxiang (R-XX), and Puyang (R-PY)). Locations of the five sites (Fig. S1) with brief descriptions are listed in Table 2. U-ZZ site is surrounded by busy roads, and two freeways are located 3 km to the south and 7 km to the east. Moreover, this site is near a coal-fired power plant; a gas-fired power plant; and several small-scale industries, such as pharmaceutical companies, electronic factories, and equipment manufacturing. U-AY site is surrounded by busy roads, and Anyang steelwork is located 8 km to the west. R-AY site is surrounded by farmland and is 1 km west of the Jing-Gang-Ao freeway and 1 km north of a belt freeway. R-XX and R-PY sites are surrounded by farmland without other prominent anthropogenic emission sources.

2.2 Instrumentations

The hourly mass concentrations of water-soluble inorganic ions (WSIIs) in $PM_{2.5}$, such as NH_4^+, SO_4^{2-}, NO_3^-, Cl^-, Na^+, Mg^{2+}, Ca^{2+}, and K^+ and their gaseous precursors (i.e., NH_3, HNO_3, and HCl) were measured using an ambient ion monitor (URG-9000D, Thermal Fisher Scientific, USA) in U-ZZ site and the monitor for aerosols and gases (MARGA, Metrohm, Switzerland) in other sites. Both instruments have been successfully deployed in several other field experiments (Li et al., 2017; Shi et al., 2017; Wang 2019b), and detailed information is available elsewhere (Markovic et al., 2012; Rumsey et al., 2014). As a brief summary, ambient air is drawn into the systems at a flow rate of 16.7 L/min. Subsequently, particles and gases are collected by two aerosol sample collectors through a wet

parallel plate or wet rotating denuder. Aqueous solution samples are quantified by using two ion chromatography analyzers. Detection limits for all species during the sampling periods were less than 0.1 $\mu g/m^3$. Measurement uncertainties were assumed to 10 % for URG-9000D here by reference to 10 % of Markovic et al. (2012) and 12 % in Hu et al. (2014). For the MARGA instrument, Song et al. (2018) took 20 % as overall relative uncertainties for major species, and Rumsey et al. (2014) reported that the analytical biases were lower than 10 % for SO_4^{2-}, NO_3^-, and HNO_3, but higher than 15 % for NH_3 and NH_4^+. Therefore, overall uncertainties were estimated to be 20 % for NH_3 and NH_4^+ and 10 % for other species. The combined uncertainties for TNH_x were calculated to be 14 % and 23 % for U-ZZ and other sites, respectively, and 14 % uncertainties of TNO_3 ($NO_{3(aq)}^- + HNO_{3(g)}$) and TCl ($Cl_{(aq)}^- + HCl_{(g)}$) for all sites. Because of the complex interference during sampling periods at the five sites, such as the slope from the internal calibration, the solution volume, temperature, pressure, and airflow rate, the actual uncertainties might be different from the estimated value. Hourly elemental carbon (EC) and organic carbon (OC) concentrations in $PM_{2.5}$ were simultaneously obtained by the semi-continuous carbon analyzers (Model 4, Sunset Laboratory Inc, USA) in the same place, except for the U-ZZ site, of which data were provided by the Department of Environmental Protection of Henan Province. Detailed information on this instrument can be found in Panteliadis et al. (2014). Briefly, $PM_{2.5}$ collected by the device was oxidized to carbon dioxide and analyzed by a nondispersive infrared detector. The relative measurement uncertainty for this instrument was estimated to be 20 % (Liu et al., 2013; Healy et al., 2013). Meteorological parameters, including T, RH, wind direction, and wind speed, were recorded by smart weather sensor (LUFFT-WS500, Sutron Corporation, Germany), with the accuracies of $\pm$ 0.2 °C, $\pm$ 2 %, < 3 °, and 0.1 m/s, respectively.

2.3 pH prediction

147

148   Particle pH was estimated using the ISORROPIA-II thermodynamic model. Input data, including

149   RH, T, concentrations of K^+, Ca^{2+}, Mg^{2+}, TNH_x, total sulfate (TH_2SO_4, replaced by observed SO_4^{2-}),

150   total sodium (TNa, replaced by observed Na^+), TCl, and TNO_3, were used to calculate the particle

151   hydronium ion concentration per volume of air (H^+_{air}) and particle water associated with inorganics

152   (AWC_{inorg}) by computing the equilibrium composition for the Na^+-K^+-Ca^{2+}-Mg^{2+}-NH_4^+-SO_4^{2-}-NO_3^--

153   Cl^--H_2O aerosol system. Considering that forward mode is less sensitive to measurement error than

154   the reverse mode and high RH levels were recorded in sampling periods, ISORROPIA-II was run in

155   the forward model for the aerosol system in the metastable condition (Ding et al, 2019; Guo et al.,

156   2015; Hennigan et al., 2015). Moreover, we excluded data with RH < 30 %, a condition where

157   predicted to observed partitioning of nitrate between the gas and particle phase are in weak correlation,

158   and thus uncertainties in the pH prediction are expected to be high (Ding et al., 2019; Guo et al., 2016).

159   Aerosol pH was calculated according to the formula (Bougiatioti et al., 2016):

$$\text{pH} = -\log_{10} H^+_{aq} = -\log_{10} \frac{1000 H^+_{air}}{AWC_{inorg} + AWC_{org}}, \tag{1}$$

160

161   where the modeled concentrations for AWC_{inorg} and H^+_{air} are $\mu g/m^3$, and AWC_{org} is the particle water

162   associated with the organics predicted using the method:

$$AWC_{org} = \frac{m_s}{\rho_s} \frac{k_{org}}{\left(\frac{1}{\text{RH}} - 1\right)}, \tag{2}$$

163

164   where m_s is the mass concentrations of organic matter (OC × 1.6), ρ_s is the organic density (1.35 g/cm^3),

165   and k_{org} is the organic hygroscopicity parameter (0.06) (Liu et al., 2017).

166 **2.4 pH uncertainty**

167   Two extreme scenarios were evaluated to estimate the pH uncertainty based on the measurement

168 uncertainties of input data (Murphy et al., 2017). Sensitivity tests of pH to input data (see Section 3.3)

169 suggest that simulated pH increase with the cation concentrations (i.e., TNH_x, TNa, K^+, Ca^{2+}, and Mg^{2+})

170 increasing as well as the anion concentrations (i.e., TH_2SO_4, TNO_3, and TCl), T and RH decreasing.

171 Moreover, the pH value has a positive correlation with OC concentrations via Eqs. (1 and 2). Therefore,

172 cation and OC concentrations were adjusted up to within their maximum positive uncertainties, and

173 anions, RH and T were adjusted down within their maximum negative uncertainties, which represented

174 the pH_{max} case; for pH_{min} case, cations and OC concentrations were adjusted down, and anions, RH

175 and T were adjusted up. Figure 1 suggests that pH_{max} cases lead to 6 % (slope − 1) errors for all sites,

176 and pH_{min} cases can result in approximately 10 % deviations. Thus, pH uncertainties were set to be

177 −9–6 %, −13–6 %, −12–6 %, −11–6 %, and −10–5 % for U-ZZ, U-AY, R-AY, R-XX, and R-PY sites,

178 respectively.

179 **2.5 Model validation**

180   The reliability of pH estimation using the ISORROPIA-II thermodynamic model depends on

181 several assumptions, such as the equilibrated gas and particle phases (Pye et al., 2019). Thus, the

182 predicted and observed semi-volatile species (e.g., $NH_{3(g)}/NH_{4(aq)}^+$, $HCl_{(g)}/Cl_{(aq)}^-$, and $HNO_{3(g)}/NO_{3(aq)}^-$)

183 are compared in Fig. S2. Observed and predicted NH_4^+, Cl^-, and NO_3^- exhibit significant correlations,

184 have correlation coefficients (r) above 0.95 and slopes near 1 at the five sites. In addition, NH_3

185 concentrations are in good agreement ($r > 0.95$) with slopes between 0.89 (U-ZZ) and 1.13 (R-PY).

186 These results suggest the excellent performance of ISORROPIA-II for modeling these species. The

9

187   differences in the slopes of NH_4^+ (Fig. S2b) and NH_3 (Fig. S2e) between U-ZZ and R-PY sites were

188   probably attributed to the unbalanced charge of input WSIIs (see Text S1 for more details of calculation)

189   with average equivalent ratios (Fig. S3) of 0.99 ± 0.13 (U-ZZ) and 1.20 ± 0.12 (R-PY). However, Song

190   et al. (2018) argued that ion balance was not a key factor for pH calculation in the forward mode,

191   because the forward mode calculations account for additional constraints imposed by the partitioning

192   of semi-volatile species. To verify this, we adjusted the measured NH_4^+ concentration, which was most

193   sensitive to pH modeling (see Section 3.3), to fit the ion balance, and reran the pH calculation. As

194   shown in Fig. S4, re-predicted NH_4^+ and NH_3 concentrations have better performance ($r = 0.99, 0.94$

195    $<$ slopes < 1.06) with input concentrations at two sites than before. However, re-calculated pH values

196   change slightly, and these deviations are included in the range of pH uncertainty discussed in Section

197   2.4. Therefore, the little differences in NH_x partitioning between the model and measurement among

198   the five sites were acceptable for pH calculation.

199   Correlations between the predicted and measured HNO_3 and HCl are weak. Similar problems

200   were found in the northeast U.S. and Beijing. These discrepancies were potentially due to measurement

201   uncertainties brought about by low gas concentrations, the interference of coarse-mode particles, non-

202   volatile cation measurement artifacts, uncertainties in the thermodynamic constants, and kinetic

203   limitations to mass transfer (Ding et al., 2019, Haskins et al., 2018; Pye et al., 2019; Liu et al., 2017).

204   Pye et al. (2019) suggested that ISORROPIA-II yields a mean activity coefficient of (H^+, Cl^-) that may

205   result in the higher predicted HCl concentration. HNO_3 can be partition to both fine and coarse modes,

206   thereby affecting predicted fine-mode nitrate concentrations (Nah et al., 2018). The best semi-volatile

207   species for evaluation of pH modeling depend on the fraction of the gas phase. In this work, most of

208   HNO$_3$ and HCl concentrated in the particle phase, and thus they are not suited to test the model (Guo

209   et al., 2016).

210   The PM$_{2.5}$ pH was also calculated by the E-AIM (Version IV) model to evaluate the performance

211   of ISORROPIA-II using the observed data (RH > 60 %) of the U-ZZ site as an example. Close

212   correlation ($r = 0.89$) is found between two models with a slope of 0.95 (Fig. S5). The pH values in

213   ISORROPIA-II are 0.46 ± 0.15 units higher than those in E-AIM. These values are comparable to the

214   founding by Liu et al. (2017) and Song et al. (2018), which is possibly due to the differences of activity

215   coefficient values between the ISORROPIA-II and E-AIM models (Pye et al., 2019). Overall, the

216   predicted pH values using ISORROPIA-II are effective in this work.

217   **3 Results and discussion**

218   **3.1 Haze episodes**

219   During the sampling periods, five monitoring sites simultaneously experienced a long-lasting and

220   large-scale haze episode. Time series of the concentrations of major species (i.e., NH$_3$, NH$_4^+$, SO$_4^{2-}$,

221   and NO$_3^-$) and meteorological parameters at the U-ZZ site as an example are presented in Fig. 2, and

222   other sites are integrated into Fig S6 with the mean values listed in Table 3. Three study cases were

223   classified on the basis of similar meteorological conditions and WSIIs levels at the five sites. The

224   WSIIs concentration, T, and RH gradually increased in the southern wind during Case 1 (January

225   12−14). Case 3 (January 21−25) was characterized by decreased WSII concentrations, T, and RH with

226   the northeastern wind. Even though the total WSIIs (TWSIIs) concentrations were comparable, the

227   chemical components of WSIIs were various between Cases 1 and 3 (Table 3). In particular, NO$_3^-$,

228   NH$_4^+$, and NH$_3$ concentrations in Case 1 were higher than those in Case 3 at all sites. Conversely,

229   SO_4^{2-} concentrations in Case 1 were lower than those in Case 3. Wang et al. (2018a) reported that the

230   southern cities of Henan Province (e.g., Nanyang, Shangqiu, Zhoukou, and Zhumadian) had relatively

231   higher ammonia emissions than the cities involved in this study. Moreover, the northeastern air masses

232   from the Jing–Jin–Ji regions were easily enriched with sulfate (Wang et al., 2019b; Wang et al., 2018c).

233   Evidently, back trajectory frequency analysis (see Text S2 for more details of the discussion) confirmed

234   that sampling sites during Cases 1 and 3 (Figs. S7a and c) were predominantly influenced by the

235   southern and northeastern air masses, respectively.

236   Elevated WSIIs concentrations during Case 2 (January 14–21) were under high T and RH

237   conditions with variable wind directions. In this case, local emissions played a key role in WSIIs (Fig.

238   S7b) with average NH_4^+, SO_4^{2-}, and NO_3^- concentrations that ranged from 31.9 ± 12.5 μg/m^3 (U-ZZ)

239   to 47.6 ± 13.1 μg/m^3 (R-AY), 32.9 ± 12.5 μg/m^3 (R-XX) to 46.8 ± 16.9 μg/m^3 (R-AY), and 58.0 ± 18.3

240   μg/m^3 (U-AY) to 76.8 ± 21.1 μg/m^3 (R-AY), respectively. Note that higher concentrations of NH_4^+,

241   NH_3, and TNH_x during Case 2 were recorded at rural sites than those at urban sites. Moreover, NH_3

242   levels in this work were higher than those in other studies summarized in Table S1. Agricultural

243   emissions, including livestock waste, N-fertilizer application, and humans, were the top three ammonia

244   contributors in Henan Province (Wang et al., 2018a), which may result in elevated ammonia

245   concentrations at rural sites.

246   **3.2 pH of PM$_{2.5}$ at the urban and rural sites**

247   Figure 3 exhibits the predicted PM$_{2.5}$ pH values, H^+_{air}, and AWC at the five sites, pH uncertainties

248   based on the pH$_{max}$ and pH$_{min}$ calculations are presented in Fig. S8. PM$_{2.5}$ have consistent moderate

249   acidity during this haze episode, with median (min–max) pH values of 4.5 (3.8–5.2), 4.8 (3.9–5.8), 4.9

250   (4.1–6.2), 5.1 (4.7–6.3), and 5.2 (4.8–6.5,) at U-ZZ, U-AY, R-XX, R-AY, and R-PY, respectively. As

251   summarized in Table 1, $PM_{2.5}$ pH values were close to the results of other cities in China (e.g., Beijing,

252   Xi'an, and Tianjin), but higher than other countries (e.g., Singapore, USA, and Greece). Compared to

253   the rural sites in the USA, pH values were roughly 3 units higher at the R-AY, R-XX, and R-PY sites.

254   Moreover, statistical values of pH (Table S2) during three cases show higher pH values at rural sites

255   than those at urban sites, especially for the U-ZZ and R-PY sites during Case 1 despite their pH

256   uncertainties (Section 2.4).

257   The pH values (Table S2) of the five sites during Cases 2 and 3 were comparable but slightly

258   lower than those during Case 1. As shown in Fig. S9, predicted pH values present better correlations

259   with H^+_{air} concentrations rather than AWC. Particle hydronium ion aqueous concentration depends on

260   both the presence of ions and the amount of particle AWC (Guo et al., 2015). Moreover, H^+_{air} was

261   closely associated with the NH_3 mixing ratios, and higher NH_3 always corresponded to lower H^+_{air} (Liu

262   et al., 2017). High correlations ($r > 0.5$) between H^+_{air} and TWSIIs (Table S3) imply that local pH was

263   significantly affected by the TWSIIs levels, and probably resulting in the high acidity during Case 2.

264   H^+_{air} was also correlated with individual chemical species (e.g., TNH_x, TH_2SO_4, TNO_3, and TCl).

265   Therefore, the diversity of pH in Cases 1 and 3 may be partly owing to the different proportions of

266   particle- and gas-phase constituents that will be discussed in detail below. In addition, high correlations

267   between RH and H^+_{air} (Table S3) suggest the major role of meteorological conditions in particle pH.

268   Given the Case 2 was less affected by regional transport, the diurnal patterns of median pH values of

269   the five sites (Fig. 4) indicate that pH values during nighttime were 0.3 (R-PY)–0.5 (U-ZZ) units higher

270   than those during the daytime. Similar results were also found in other cities (e.g., Beijing, Tianjin,

13

271   southern Canada, and the USA) (Battaglia et al., 2017; Ding et al., 2019; Guo et al., 2015; Murphy et

272   al., 2017; Shi et al., 2019), resulting from the diurnal trends of T and RH (Fig. 4f). After sunrise, high

273   T facilitated the dissociation of particle-phase ammonium (e.g., NH_4NO_3) and led to a rapid loss of

274   AWC (Guo et al., 2015; Saraswati et al., 2019).

275   **3.3 Sensitivity tests of pH**

276   To explore the dominant factors that determine the local particle pH level and resulting in the high

277   pH at rural sites, sensitivity tests of pH to chemical species (i.e., TNH_x, TH_2SO_4, TNO_3, TCl, TNa, K^+,

278   Ca^{2+}, and Mg^{2+}) and meteorological parameters (i.e., T and RH) were performed. Firstly, the real-time

279   measured values of a variable (e.g., TNH_x) and average values of other parameters (i.e., TH_2SO_4, TNO_3,

280   TCl, TNa, K^+, Ca^{2+}, Mg^{2+}, T and RH) during Case 2 were input into ISORROPIA-II to investigate the

281   sensitivity of local pH to this variable (i.e., TNH_x) (Ding et al., 2019), and results are listed in Table 4

282   and Fig. S10. In addition, a given range for a variable for all sites with corresponding average values

283   of other parameters was simulated to compare its effects on pH among five sites (Figs. 5 and S11). The

284   chosen variation range for each variable was close to the observed minimum and maximum values

285   (Table S4), which aims to better reflect the actual observation conditions. The degree of sensitivity

286   was represented as the relative standard deviation (%RSD) of the re-calculated pH values. RSD

287   calculates the absolute value of the coefficient of variation, which helps us to determine how small or

288   large is the standard deviation when compared to the mean of the re-calculated pH data set. Therefore,

289   when the re-calculated pH data set has a higher RSD value, this variable can change the pH easier and

290   is more important for local pH.

291   As shown in Table 4, the most important factor that influenced particle pH during Case 2 was

14

292   TNH_x, followed by TH_2SO_4 at the five sites, and the U-ZZ site was also affected by TNO_3. The acidity

293   of $PM_{2.5}$ is governed by the phase partitioning of semi-volatile gases such as NH_3, HNO_3, and HCl

294   (Pye et al., 2019). $(NH_4)_2SO_4$, NH_4HSO_4, and NH_4NO_3, which are mainly formed through

295   neutralization reactions between NH_3 with SO_4^{2-} and HNO_3 orderly according to the regime of local

296   ammonia, are the most abundant components of $PM_{2.5}$ in winter haze in this region (Wang et al., 2019c;

297   Pathak et al., 2008). Therefore, particle pH was driven by TNH_x, TH_2SO_4, and TNO_3. TNa, TCl, and

298   crustal ions (i.e., K^+, Ca^{2+}, and Mg^{2+}) have less influence on the predicted pH values, because these

299   species were at low concentrations, together accounting for lower than 10 % of TWSIIs. However,

300   since the low volatility of these cations allows them to preferentially neutralize sulfates over NH_3, the

301   role of crustal dust and sea spray in particle pH cannot be ignored when the mass fraction of these ions

302   are high in typical pollution events (e.g., sandstorm) or areas (e.g., coastland) (Allen et al., 2015; Guo

303   et al., 2018; Vasilakos et al., 2018). In addition to chemical species, T was more sensitive to local pH

304   than RH at the five sites, which is similar to the finding in Beijing and Canada (Ding et al., 2019; Tao

305   and Murphy, 2019). This result can be explained by the remarkable influence of T on the solubility and

306   dissociation constants of the partitioning of $NH_{3(g)}/NH_{4(aq)}^+$ (Hennigan et al., 2015).

307   Figures 5 and S11 compare the sensitive degrees of pH to input data among different sites. Except

308   for TNH_x, the sensitivities of pH to TH_2SO_4, TNO_3, and other ions at urban sites were more significant

309   than those at rural sites, particularly at U-ZZ sites of 7.2 % and 14.8 % of RSD to TH_2SO_4 and TNO_3,

310   respectively. To gain insight into the differences of pH sensitivity among the five sites, sensitivity tests

311   of pH to TH_2SO_4, TNO_3, and TNH_x were calculated using the fixed TNO_3 (67.5 μg/m^3) and TH_2SO_4

312   (36.5 μg/m^3) concentrations under the average meteorological conditions of five sites (i.e., T = 2.5 °C

313 and RH = 60 %). These chosen values were close to the average values of the five sites during Case 2

314 (i.e., 36.4 ± 15.4 μg/m^3 for SO_4^{2-}, 67.5 ± 23.5 μg/m^3 for TNO_3, 2.5 ± 1.5 °C for T, and 59.3 ± 14.0 %

315 for RH), and other chemical species were set to be zero. As shown in Fig. 6, sensitivities of pH to

316 TH_2SO_4 and TNO_3 increase with the decrease in TNH_x concentration, particularly when the TNH_x

317 concentrations are lower than 60 μg/m^3 and 40 μg/m^3, respectively. Therefore, the pH changes tended

318 to become more sensitive to TH_2SO_4 and TNO_3 at the U-ZZ site (Fig. 5e, f) with the lowest TNH_x

319 concentrations (46.8 ± 14.7 μg/m^3). All these results may be explained by the presence of excess

320 ammonia that will be discussed below.

321   Sensitivity tests suggest (Fig. 5, S10, and S11) that particle pH gradually grows with increased

322 cation and decreased anion concentrations. Specifically, the TNH_x concentration that increased from

323 25 μg/m^3 to 90 μg/m^3 can promote particle pH by 3.5 (U-ZZ)–4.5 (R-AY) units. The crustal cations

324 and sea spray have limited effects on pH, but a 10-fold increase in these species still can increase

325 predicted pH values by about 0.1 units. TH_2SO_4, and TNO_3 that increased from 10 μg/m^3 to 80 μg/m^3,

326 and 1 μg/m^3 to 125 μg/m^3 can reduce the pH values by 1.5 (R-PY)–4.0 (U-ZZ), and 0.2 (R-AY)–1.4

327 (U-ZZ) units, respectively. In addition, a 20 °C (–5 °C to 15 °C) and 65 % (30 % to 95 %) increase

328 drops the pH by approximately 1.3 and 2.7 units at the five sites, respectively. Corresponding to the

329 observed data during Case 2 (Table 3), lower TNH_x concentrations and higher T values were probably

330 responsible for the higher acidity at urban sites than those at rural sites. Moreover, Figure 6 shows that

331 particle pH increase with decreasing TH_2SO_4 (Fig. 6a) or increasing TNO_3 (Fig. 6b), particularly when

332 the TNH_x is at high concentration. These results indicate that predicted pH will be enhanced by

333 increasing the TNO_3/TH_2SO_4 ratio, which is consistent with the observation in Beijing (Xie et al.,

334 2019). All these may be due to the elevated ammonia partitioning with nitrate fraction increase, and

335 nitrate-rich particles would absorb more water compared to the sulfate-rich particles (Xie et al., 2019).

336 Based on the above, higher TNH_x (Table 3) and TNO_3/TH_2SO_4 ratios (2.9 ± 0.6 and 1.7 ± 0.6 for Cases

337 1 and 3 respectively) during Case 1 may lead to the higher pH values than those during Case 3, even

338 though the TWSIIs levels were comparable. In the long run, the decreasing sulfate concentration in

339 $PM_{2.5}$ accompanied with increasing nitrate concentration has been recorded during haze episodes in

340 China, because strong actions were taken to reduce the coal consumption in recent years (Tian et al.,

341 2017; Wang et al., 2017). Considering the ammonia in the atmosphere of North China might still be

342 increasing (Liu et al., 2018), future acidity of $PM_{2.5}$ during winter haze episodes is expected to become

343 increasingly less acidic in this area. A more careful analysis is needed to test this inference, however,

344 because fine-mode particle remains a relatively constant pH of 0–2 despite a 70 % reduction in sulfates

345 in the USA (Vasilakos et al., 2018; Weber et al., 2016).

346 **3.4 Role of ammonia on pH**

347 It has been suggested that unusually high levels of NH_3 can increase pH, on average, a 5-fold to

348 10-fold increase in the NH_3 levels leads to a one-unit change in pH (Nah et al., 2018; Weber et al.,

349 2016; Guo et al., 2017). To examine the effects of major indicators of ammonia (i.e., TNH_x, Required-

350 NH_x, and Excess-NH_x, see Text S3 for more details of calculation) on aerosol acidity, particle pH was

351 calculated by using a wide range of TNH_x (25–130 $\mu g/m^3$) and average values of other parameters

352 during Case 2 (Table 3) of each site. Simultaneously, the concentrations of TNH_x, Required-NH_x,

353 Excess-NH_x, and corresponding pH values are illustrated in Fig. 7. An "*S*-curve" growth trend of pH

354 to increasing TNH_x appears with the inflection point around the Required-NH_x concentration. In the

355 case when the input TNH_x concentration is lower than the Required-NH_x, the growth rate of pH

356 increase with TNH_x increasing, otherwise, the pH growth flattens out, which is similar to the findings

357 of Weber et al. (2016) and Bougiatioti et al. (2016). In the process of increasing NH_3 concentration,

358 NH_3 reacted with SO_4^{2-} and HNO_3 orderly, during when large amounts of H^+ were consumed and pH

359 values rapidly increased. Theoretically, the Required-NH_x plus nonvolatile cations can neutralize all

360 anions regardless of the phase partitioning and bisulfate formation, and thus changes in TNH_x around

361 the Required-NH_x concentrations have a significant impact on particle pH. Subsequently, dissolving

362 Excess-NH_x into the particles became difficult, and pH values increased slowly (Ding et al., 2019;

363 Seinfeld and Pandis, 2016). Therefore, the underlying reason why TNH_x concentrations lower than 60

364 $\mu g/m^3$ and 40 $\mu g/m^3$ elevated the pH sensitivities (Fig. 6) to TH_2SO_4 and TNO_3 is that the Excess-NH_x

365 will be exhausted under the case of TH_2SO_4 and TNO_3 that ranged from 10 $\mu g/m^3$ to 100 $\mu g/m^3$,

366 respectively. On the other hand, the pH values of the five sites at the Required-NH_x concentrations are

367 near 3.0, which is in coincidence with the pH value of Beijing in the no-excess-NH_x cases (Liu et al.,

368 2017). Therefore, the presence of Excess-NH_x in the aerosol was likely important for the less acidic of

369 $PM_{2.5}$ and can enhance the pH values by 1.5 (U-ZZ)–2 (R-PY) units. Considering that the Excess-NH_x

370 concentrations at rural sites (e.g., 30.1 ± 6.2 $\mu g/m^3$ at R-PY) were higher than those at urban sites (e.g.,

371 14.8 ± 4.1 $\mu g/m^3$ at U-ZZ), and thus Excess-NH_x concentrations may drive the pH values of rural sites

372 higher than those of urban sites.

373 **3.5 Implications of regional transport**

374 From the above discussion, the differences of pH among three cases indicate that the underlying

375 influence of regional transport on local particle pH cannot be neglected by differing the chemical

18

376   components of $PM_{2.5}$ and meteorological conditions. In particular, the median pH values (Table S2) of

377   Case 1, during when the air masses transported from the south of sampling regions, increased by 0.2–

378   0.9 units than those during Cases 2 and 3. Aqueous formations of sulfate are strongly dependent on

379   particle pH. Chen et al. (2016) reported that the aqueous-phase sulfate production rates from NO_2 and

380   O_3 oxidation of SO_2 had a positive correlation with particle pH during the Beijing haze events. When

381   pH exceeded approximately 4.5 (higher than this value at rural sites in this work), NO_2-oxidation

382   dominated the sulfate formation, and its reaction rate increased by one order of magnitude with the

383   rise of pH by one unit. Thus, air masses transported from rural and agricultural regions may promote

384   the sulfate formation in urban aerosols. In addition to sulfate, higher aerosol pH favors partitioning of

385   TNO_3 toward aerosol NO_3 rather than gaseous HNO_3 and thus elevating the particle mass

386   concentration (Nenes et al., 2019; Weber et al., 2016). Sampling regions in this study are located in the

387   transport route for Beijing (MEP, 2017), thereby frequently affecting its local particle pH. The lifetimes

388   of NH_3 (1–5 days or less) and NH_4^+ (1–15 days) in the atmosphere are sufficient for transporting to

389   Beijing during a haze episode (Aneja, 2000; Lefer et al., 1999; Warneck, 1988). Ding et al. (2019)

390   have also observed that $PM_{2.5}$ pH from the southwest direction was generally higher than that from the

391   northern direction in Beijing. Therefore, the particle pH in Beijing may be enhanced when southern

392   air masses from this region accompany elevated-pH particles and high ammonia levels.

393   **4 Conclusions**

394   An experiment was performed using a series of high-time-resolution instruments in two urban

395   (i.e., U-ZZ and U-AY) and three rural sites (i.e., R-AY, R-XX, and R-PY) in Henan Province during a

396   large-scale and long-lasting haze episode. The ISORROPIA-II model was used to investigate the pH

397 value and its driving factors. $PM_{2.5}$ exhibited moderate acidity with median pH values of 4.5 (3.8–5.2),

398 4.8 (3.9–5.8), 4.9 (4.1–6.2), 5.1 (4.7–6.3), and 5.2 (4.8–6.5,) at U-ZZ, U-AY, R-XX, R-AY, and R-PY,

399 respectively. The pH values at rural sites were slightly higher than those at urban sites.

400 The predicted pH values of $PM_{2.5}$ were significantly affected by the WSIIs levels, different

401 proportions of particle- and gas-phase constituents, and meteorological parameters. Sensitivity tests

402 show that TNH_x, followed by TH_2SO_4, were the important factors that influenced the predicted pH at

403 the five sites. In addition, T was more sensitive to local pH than RH. Generally, particle pH rose with

404 the increase in cation and the decrease in the anion, T, and RH. Further study suggests that predicted

405 pH will be enhanced by increasing the TNO_3/TH_2SO_4 ratio. Therefore, elevated TNH_x concentrations

406 and lower T were probably responsible for the higher pH values at rural sites than those at urban sites,

407 and higher TNH_x and TNO_3/TH_2SO_4 ratios during Case 1 may lead to the higher pH values than those

408 during Case 3.

409 An "S-curve" growth trend of pH to increasing TNH_x was found with the inflection point around

410 the Required-NH_x concentration. Moreover, the pH values of the five sites at the Required-NH_x

411 concentrations are near 3.0, and the presence of Excess-NH_x in the aerosol can enhance the pH values

412 by 1.5 (U-ZZ)–2 (R-PY) units, and thus Excess-NH_x was likely important for the less acidic of $PM_{2.5}$

413 during the severe haze episodes in this region. Considering that the Excess-NH_x concentrations at rural

414 sites were higher than those at urban sites, Excess-NH_x concentrations may drive the pH values of rural

415 sites higher than those of urban sites.

416 The underlying influence of regional transport on local particle pH cannot be neglected by

417 differing the chemical components of $PM_{2.5}$ and meteorological conditions. Air masses transported

20

418   from rural and agricultural regions with elevated pH particles and high ammonia levels may promote

419   the secondary particle formation in urban aerosols. Therefore, ammonia should be involved in the

420   regional strategy for improving the air quality in China.

421

422   *Data availability. All data in this work are available by contacting the corresponding author Shasha*

423   *Yin (shashayin@zzu.edu.cn)*

424

425   *Author contributions. Shasha Yin and Ruiqin Zhang designed and led this study. Shasha Yin was*

426   *responsible for all observations and data collection. Lingling Wang, Yuqing Li, Chen Wang, and Weisi*

427   *Wang interpreted the data and discussed the results. Shenbo Wang wrote the paper.*

428

429   *Competing interests. The authors declare that they have no conflict of interest.*

434   **References**

435   Allen, H. M., Draper, D. C., Ayres, B. R., Ault, A., Bondy, A., Takahama, S., Modini, R. L., Baumann,

436   K., Edgerton, E., Knote, C., Laskin, A., Wang, B., and Fry, J. L.: Influence of crustal dust and sea

437   spray supermicron particle concentrations and acidity on inorganic NO_3^- aerosol during the 2013

438   Southern Oxidant and Aerosol Study. Atmos. Chem. Phy., 15, 10669−10685, 2015.

439   Aneja, V. P., Chauhan, J. P., Walker, J. T.: Characterization of atmospheric ammonia emissions from

440   swine waste storage and treatment lagoons. J. Geophy. Res.-Atmos., 105, 11535−11545, 2000.

441   Battaglia, M. A., Douglas, S., and Hennigan, C. J.: Effect of the urban heat island on aerosol pH,

442   Environ. Sci. Technol., 51, 13095−13103, 2017.

443   Behera, S. N., Betha, R., Liu, P., Balasubramanian, R.: A study of diurnal variations of $PM_{2.5}$ acidity

444   and related chemical species using a new thermodynamic equilibrium model. Sci. Total Environ.,

445   452, 286−295, 2013.

446   Boucher, O., Anderson, T. L.: General circulation model assessment of the sensitivity of direct climate

447   forcing by anthropogenic sulfate aerosols to aerosol size and chemistry. J. Geophy. Res.-Atmos.,

448   100, 26117−26134, 1995.

449   Bougiatioti, A., Nikolaou, P., Stavroulas, I., Kouvarakis, G., Weber, R., Nenes, A., Kanakidou, M.,

450   Mihalopoulos, N.: Particle water and pH in the eastern Mediterranean: source variability and

451   implications for nutrient availability. Atmos. Chem. Phy., 16, 4579−4591, 2016.

452   Bureau of Statistics of Henan (NBH), 2018. Henan Statistical Yearbook. China Statistics Press, Beijing.

453   Accessed date: Dec. 2019.

454   Cheng, Y., Zheng, G., Wei, C., Mu, Q., Zheng, B., Wang, Z., Gao, M., Zhang, Q., He, K., Carmichael,

455   G.: Reactive nitrogen chemistry in aerosol water as a source of sulfate during haze events in China.

456   Sci. Adv., 2, e1601530−e1601530, 2016.

457   Clegg, S. L., Brimblecombe, P., Wexler, A. S.: The thermodynamic model of the system

458   H^+−NH_4^+−SO_4^{2-}−NO_3^-−H_2O at tropospheric temperatures. J. Phy. Chem. A, 102, 2137−2154,

459   1998.

460   Ding, J., Zhao, P., Su, J., Dong, Q., Du, X., Zhang, Y.: Aerosol pH and its driving factors in Beijing.

461   Atmos. Chem. Phy., 19, 7939−7954, 2019.

462   Dockery, D. W., Cunningham, J., Damokosh, A. L., Neas, L. M., Spengler, J. D., Koutrakis, P., Ware,

463   J. H., Raizenne, M., Speizer, F. E.: Health effects of acid aerosols on North American children:

464   respiratory symptoms. Environ. Health Persp., 104, 500−505, 1996.

465   Guo, H., Sullivan, A. P., Campuzanojost, P., Schroder, J. C., Lopezhilfiker, F. D., Dibb, J. E., Jimenez,

466   J. L., Thornton, J. A., Brown, S. S., Nenes, A.: Fine particle pH and the partitioning of nitric acid

467   during winter in the northeastern United States. J. Geophy. Res.-Atmos., 121, 10−355, 2016.

468   Guo, H., Weber, R. J., Nenes, A.: High levels of ammonia do not raise fine particle pH sufficiently to

469   yield nitrogen oxide-dominated sulfate production. Sci. Rep., 7, 12109, 2017.

470   Guo, H., Xu, L., Bougiatioti, A., Cerully, K. M., Capps, S. L., Hite, J. R., Carlton, A. G., Lee, S., Bergin,

471   M. H., Ng, N. L.: Fine-particle water and pH in the southeastern United States. Atmos. Chem.

472   Phy., 15, 5211−5228, 2015.

473   Guo, H., Nenes, A., and Weber, R. J.: The underappreciated role of nonvolatile cations on aerosol

474   ammonium-sulfate molar ratios, Atmos. Chem. Phys., 18, 17307–17323, 2018.

475   Haskins, J. D., Jaegle, L., Shah, V., Lee, B. H., Lopez-Hilfiker, F. D., Campuzano-Jost, P., Schroder, J.

476   C., Day, D. A., Guo, H. Y., Sullivan, A. P., Weber, R., Dibb, J., Campos, T., Jimenez, J. L., Brown,

477   S. S., and Thornton, J. A.: Wintertime gas-particle partitioning and speciation of inorganic

478   chlorine in the lower troposphere over the northeast United States and coastal ocean, J. Geophys.

479   Res.-Atmos., 123, 12897−12916, 2018

480   Healy, R. M., Sciare, J., Poulain, L., Crippa, M., Wiedensohler, A., Prévôt, A. S. H., Baltensperger, U.,

481   Sarda-Estève, R., McGuire, M. L., Jeong, C.-H., McGillicuddy, E., O'Connor, I. P., Sodeau, J. R.,

482   Evans, G. J., and Wenger, J. C.: Quantitative determination of carbonaceous particle mixing state

483   in Paris using single-particle mass spectrometer and aerosol mass spectrometer measurements,

484   Atmos. Chem. Phys., 13, 9479–9496, 2013.

485 Hennigan, C. J., Izumi, J., Sullivan, A. P., Weber, R. J., and Nenes, A.: A critical evaluation of proxy

486   methods used to estimate the acidity of atmospheric particles, Atmos. Chem. Phys., 15, 2775–

487   2790, 2015.

488 Hu, G., Zhang, Y., Sun, J., Zhang, L., Shen, X., Lin, W., Yang, Y.: Variability, formation and acidity of

489   water-soluble ions in $PM_{2.5}$ in Beijing based on the semi-continuous observations. Atmos. Res.,

490   145, 1−11, 2014.

491 Huang, X., Song, Y., Li, M., Li, J., Huo, Q., Cai, X., Zhu, T., Hu, M., Zhang, H.: A high-resolution

492   ammonia emission inventory in China. Global Biogeochem. Cy., 26, GB1030, 2012.

493 Larssen, T., Lydersen, E., Tang, D., He, Y., Gao, J., Liu, H., Duan, L., Seip, H .M., Vogt, R. D., Mulder,

494   J.: Acid rain in China. Environ. Sci. Technol., 40, 418−425, 2006.

495 Lefer, B. L., Talbot, R. W., Munger, J. W.: Nitric acid and ammonia at a rural northeastern US site. J.

496   Geophy. Res.-Atmos., 104, 1645−1661, 1999.

497 Li, Y. J., Sun, Y., Zhang, Q., Li, X., Li, M., Zhou, Z., Chan, C. K.: Real-time chemical characterization

498   of atmospheric particulate matter in China: A review. Atmos. Environ., 158, 270−304, 2006.

499 Liu, J., Bergin, M., Guo, H., King, L., Kotra, N., Edgerton, E., Weber, R. J.: Size-resolved

500   measurements of brown carbon in water and methanol extracts and estimates of their contribution

501   to ambient fine-particle light absorption. Atmos. Chem. Phy., 13, 12389−12404, 2013.

502   Liu, M., Song, Y., Zhou, T., Xu, Z., Yan, C., Zheng, M., Wu, Z., Hu, M., Wu, Y., Zhu, T.: Fine particle

503   pH during severe haze episodes in northern China. Geophys. Res. Lett., 44, 5213−5221, 2017.

504   Liu, W., Lin, S., and Hu, G.: Characterizing remarkable changes of severe haze events and chemical

505   compositions in multi-size airborne particles (PM_1, $PM_{2.5}$ and PM_{10}) from January 2013 to

506   2016−2017 winter in Beijing, China, Atmos. Environ., 189, 133−144, 2018.

507   Markovic, M. Z., Vandenboer, T. C., Murphy, J. G.: Characterization and optimization of an online

508   system for the simultaneous measurement of atmospheric water-soluble constituents in the gas

509   and particle phases. J Environ. Monitor., 14, 1872−1884, 2012.

510   Meng, Z., Lin, W., Jiang, X., Yan, P., Wang, Y., Zhang, Y. M., Jia, X. F., Yu, X. L.: Characteristics of

511   atmospheric ammonia over Beijing, China. Atmos. Chem. Phy., 11, 6139−6151, 2011.

512   Meng, Z., Xu, X., Lin, W., Ge, B., Xie, Y., Song, B., Jia, S., Zhang, R., Peng, W., Wang, Y.: Role of

513   ambient ammonia in particulate ammonium formation at a rural site in the North China Plain.

514   Atmos. Chem. Phy., 18, 167−184, 2017.

515   MEP: 2017 air pollution prevention and management plan for the Beijing-Tianjin-Hebei region and its

516   surrounding areas, http://dqhj.mee.gov.cn/dtxx/201703/t20170323_408663.shtml (last access: 18

517   August 2019), 2017.

518   Meskhidze, N., Chameides, W. L., Nenes, A., Chen, G.: Iron mobilization in mineral dust: Can

519   anthropogenic SO_2 emissions affect ocean productivity? Geophys. Res. Lett., 30, 2003.

520   Murphy, J. G., Gregoire, P. K., Tevlin, A. G., Wentworth, G. R., Ellis, R. A., Markovic, M. Z.,

521   VandenBoer, T. C.: Observational constraints on particle acidity using measurements and

522   modelling of particles and gases, Faraday Discuss., 200, 379−395, 2017.

523   Nah, T., Guo, H., Sullivan, A. P., Chen, Y., Tanner, D. J., Nenes, A., Russell, A., Ng, L. N., Huey, L.

524   G., Weber, R. J.: Characterization of aerosol composition, aerosol acidity, and organic acid

525   partitioning at an agriculturally intensive rural southeastern US site. Atmos. Chem. Phy. 18,

526   11471−11491. 2018.

527   National Bureau of Statistics (NBS), 2016. China Statistical Yearbook. China Statistics Press, Beijing.

528   Accessed date: Sept. 2019.

529   Nenes, A., Pandis, S. N., Pilinis, C.: ISORROPIA: A new thermodynamic equilibrium model for

530   multiphase multicomponent inorganic aerosols. Aquat. Geochem., 4, 123−152, 1998.

531   Nenes, A., Pandis, S. N., Weber, R. J., and Russell, A.: Aerosol pH and liquid water content determine

532   when particulate matter is sensitive to ammonia and nitrate availability, Atmos. Chem. Phys.

533   Discuss., in review, 2019.

534   Ostro, B., Lipsett, M., Wiener, M.B., Selner, J.C.: Asthmatic responses to airborne acid aerosols. Am.

535   J. Public Health, 81, 694−702, 1991.

536   Panteliadis, P., Hafkenscheid, T., Cary, B., Diapouli, E., Fischer, A., Favez, O., Quincey, P., Viana, M.,

537   Hitzenberger, R., Vecchi, R.: ECOC comparison exercise with identical thermal protocols after

538   temperature offset correction: instrument diagnostics by in-depth evaluation of operational

539   parameters. Atmos. Meas. Tech., 8, 779−792, 2014.

540   Pathak, R. K., Louie, P. K., Chan, C. K.: Characteristics of aerosol acidity in Hong Kong. Atmos.

541   Environ., 38, 2965−2974, 2004.

542   Pathak, R.K., Wu, W.S., Wang, T.: Summertime $PM_{2.5}$ ionic species in four major cities of China:

543   nitrate formation in an ammonia-deficient atmosphere. Atmos. Chem. Phys. 9, 1711–1722, 2008.

544   Pye, H. O. T., Nenes, A., Alexander, B., Ault, A. P., Barth, M. C., Clegg, S. L., Collett Jr., J. L., Fahey,

545   K. M., Hennigan, C. J., Herrmann, H., Kanakidou, M., Kelly, J. T., Ku, I.-T., McNeill, V. F.,

546   Riemer, N., Schaefer, T., Shi, G., Tilgner, A., Walker, J. T., Wang, T., Weber, R., Xing, J., Zaveri,

547   R. A., and Zuend, A.: The acidity of atmospheric particles and clouds, Atmos. Chem. Phys.

548   Discuss., in review, 2019.

549   Rumsey, I. C., Cowen, K. A., Walker, J. T., Kelly, T. J., Hanft, E. A., Mishoe, K., Rogers, C., Proost,

550   R., Beachley, G. M., Lear, G.: An assessment of the performance of the Monitor for AeRosols

551   and GAses in ambient air (MARGA): a semi-continuous method for soluble compounds. Atmos.

552   Chem. Phy., 14, 5639−5658, 2014.

553   Saraswati, Sharma, S. K., Saxena, M., Mandal, T. K.: Characteristics of gaseous and particulate

554   ammonia and their role in the formation of secondary inorganic particulate matter at Delhi, India.

555   Atmos. Res., 218, 34−49, 2019.

556   Seinfeld, J. H. and Pandis, S. N.: Atmospheric Chemistry and Physics: From Air Pollution to Climate

557   Change, 2nd Edition, John Wiley and Sons, Inc., Hoboken, New Jersey, USA, 2006.

558   Seinfeld, J. H. and Pandis, S. N.: Atmospheric Chemistry and Physics: From Air Pollution to Climate

559   Change (3rd edition), John Wiley and Sons, Inc., Hoboken, New Jersey, USA, 2016.

560   Shen, J., Liu, X., Ying, Z., Fangmeier, A., Goulding, K., Zhang, F.: Atmospheric ammonia and

561   particulate ammonium from agricultural sources in the North China Plain. Atmos. Environ., 45,

562   5033−5041, 2011.

563   Shi, G., Xu, J., Peng, X., Xiao, Z., Chen, K., Tian, Y., Guan, X., Feng, Y., Yu, H., Nenes, A.: pH of

564   aerosols in a polluted atmosphere: source contributions to highly acidic aerosol. Environ. Sci.

565   Technol., 51, 4289−4296, 2017.

566   Shi, X., Nenes, A., Xiao, Z., Song, S., Yu, H., Shi, G., Zhao, Q., Chen, K., Feng, Y., Russell, A. G.:

567   High-resolution data sets unravel the effects of sources and meteorological conditions on nitrate

568   and its gas-particle partitioning. Environ. Sci. Technol., 53, 3048−3057, 2019.

569   Shi, Z., Bonneville, S., Krom, M. D., Carslaw, K. S., Jickells, T. D., Baker, A. R., Benning, L. G.: Iron

570   dissolution kinetics of mineral dust at low pH during simulated atmospheric processing. Atmos.

571   Chem. Phy., 11, 995−1007, 2010.

572   Song, S., Gao, M., Xu, W., Shao, J., Shi, G., Wang, S., Wang, Y., Sun, Y., Mcelroy, M. B.: Fine particle

573   pH for Beijing winter haze as inferred from different thermodynamic equilibrium models. Atmos.

574   Chem. Phy., 18, 7423−7438, 2018.

575   Spurny, K. R.: Atmospheric acidic aerosols (review). J Aerosol Sci., 21, 1990.

576   Surratt, J. D., Chan, A. W. H., Eddingsaas, N. C., Chan, M. N., Loza, C. L., Kwan, A. J., Hersey, S.,

577   Flagan, R. C., Wennberg, P. O., Seinfeld, J. H.: Reactive intermediates revealed in secondary

578   organic aerosol formation from isoprene. P. Natl. Acad. Sci. USA., 107, 6640−6645, 2010.

579   Tao, Y. and Murphy, J. G.: The sensitivity of $PM_{2.5}$ acidity to meteorological parameters and chemical

580   composition changes: 10-year records from six Canadian monitoring sites. Atmos. Chem. Phy..

581   19, 9309−9320, 2019.

582   Tian, M., Wang, H., Chen, Y., Zhang, L., Shi, G., Liu, Y., Yu, J., Zhai, C., Wang, J., Yang, F.: Highly

583   time-resolved characterization of water-soluble inorganic ions in $PM_{2.5}$ in a humid and acidic

584   mega city in Sichuan Basin, China. Sci. Total Environ., 580, 224−234, 2017.

585   Vasilakos, P., Russell, A., Weber, R., and Nenes, A.: Understanding nitrate formation in a world with

586   less sulfate, Atmos. Chem. Phys., 18, 12765–12775, 2018.

587   Wang, C., Yin, S., Bai, L., Zhang, X., Gu, X., Zhang, H., Lu, Q., Zhang, R.: High-resolution ammonia

588   emission inventories with comprehensive analysis and evaluation in Henan, China, 2006–2016.

589   Atmos. Environ., 193, 11−23, 2018a.

590   Wang, G., Zhang, F., Peng, J., Duan, L., Ji, Y., Marreroortiz, W., Wang, J., Li, J., Wu, C., Cao, C.:

591   Particle acidity and sulfate production during severe haze events in China cannot be reliably

592   inferred by assuming a mixture of inorganic salts. Atmos. Chem. Phy., 18, 1−23, 2018b.

593   Wang, G., Zhang, R., Gomez, M. E., Yang, L., Levy, Z. M., Hu, M., Lin, Y., Peng, J., Guo, S., Meng,

594   J.: Persistent sulfate formation from London Fog to Chinese haze. P. Natl. Acad. Sci. USA., 113,

595   13630−13635, 2016.

596   Wang, H., Ding, J., Xu, J., Wen, J., Han, J., Wang, K., Shi, G., Feng, Y., Ivey, C., Wang, Y.: Aerosols

597   in an arid environment: The role of aerosol water content, particulate acidity, precursors, and

598   relative humidity on secondary inorganic aerosols. Sci. Total Environ., 646, 564−572, 2019a.

599   Wang, J., Zhao, B., Wang, S., Yang, F., Xing, J., Morawska, L., Ding, A., Kulmala, M., Kerminen, V.,

600   Kujansuu, J.: Particulate matter pollution over China and the effects of control policies. Sci. Total

601   Environ., 584, 426−447, 2017.

602   Wang, S., He, B., Yuan, M., Su, F., Yin, S., Yan, Q., Jiang, N., Zhang, R., Tang, X.: Characterization

603   of individual particles and meteorological conditions during the cold season in Zhengzhou using

604   a single particle aerosol mass spectrometer. Atmos. Res., 219, 13−23, 2019b.

605   Wang, S., Yan, Q., Yu, F., Wang, Q., Yang, L., Zhang, R., Yin, S., Wang, S., Yan, Q., Yu, F.: Distribution

606   and source of chemical elements in size-resolved particles in Zhengzhou, China: Effects of

607   regional transport. Aerosol Air Qual. Res., 18, 371−385, 2018c.

608 Wang, S., Yin, S., Zhang, R., Yang, L., Zhao, Q., Zhang, L., Yan, Q., Jiang, N., Tang, X.: Insight into

609   the formation of secondary inorganic aerosol based on high-time-resolution data during haze

610   episodes and snowfall periods in Zhengzhou, China. Sci. Total Environ., 660, 47−56, 2019c.

611 Warneck, P.: Chemistry of the Natural Atmosphere, Academic Press, San Diego, CA, 1988.

612 Watson, J. G.: Visibility: science and regulation. J Air Waste Manage., 52, 973−999, 2002.

613 Weber, R. J., Guo, H., Russell, A. G., and Nenes, A.: High aerosol acidity despite declining

614   atmospheric sulfate concentrations over the past 15 years, Nat. Geosci., 9, 282−285, 2016.

615 Wen, L., Chen, J., Yang, L., Wang, X., Xu, C., Sui, X., Yao, L., Zhu, Y., Zhang, J., Zhu, T.: Enhanced

616   formation of fine particulate nitrate at a rural site on the North China Plain in summer: The

617   important roles of ammonia and ozone. Atmos. Environ., 101, 294−302, 2015.

618 Xie, Y., Wang, G., Wang, X., Chen, J., Chen, Y., Tang, G., Wang, L., Ge, S., Xue, G., Wang, Y., and

619   Gao, J.: Observation of nitrate dominant $PM_{2.5}$ and particle pH elevation in urban Beijing during

620   the winter of 2017, Atmos. Chem. Phys. Discuss., in review, 2019.

621

Figure lists:

Fig. 1 pH uncertainties of the five sites based on two extreme scenarios of measurement uncertainty. Cations and organic carbon concentrations (OC) were adjusted up to within their maximum positive uncertainties, anions, relative humidity (RH) and temperature (T) were adjusted down within their maximum negative uncertainties, which represented the pH_{max} case; for pH_{min} case, cations and OC concentrations were adjusted down, and anions, RH and T were adjusted up. The color scale bar represents adjusted RH.

Fig. 2 Temporal variations of T, RH, wind speed (WS), wind direction (WD), and concentrations of NH_3, NH_4^+, SO_4^{2-}, and NO_3^- during three cases at the Zhengzhou (U-ZZ) site. The shaded areas represent the measurement uncertainties.

Fig. 3 Time series and box plot of predicted $PM_{2.5}$ pH, H^+_{air}, and aerosol water content (AWC) at the five sites. In each box, the top, middle and bottom lines represent the 75th, 50th, and 25th percentile of statistical data, respectively; the upper and lower whiskers represent the maximum and minimum values, respectively.

Fig. 4 (a)–(e) Diurnal patterns of median pH values, (f) average RH, and T of the five sites in Case 2. The upper and lower ends of the line represent the maximum and minimum values of pH, respectively. The color scale bar represents AWC concentration.

Fig. 5 Comparison of the sensitivities of $PM_{2.5}$ pH to T, RH, TCl ($HCl_{(g)}$ + $Cl_{(aq)}^-$), TNH_x ($NH_{3(g)}$ + $NH_{4(aq)}^+$), TNO_3 ($HNO_{3(g)}$ + $NO_{3(aq)}^-$), and TH_2SO_4 (replaced by observed SO_4^{2-}) among the five sites. A given range for a variable for all sites with corresponding average values of other parameters was used as input to the ISORROPIA-II model. The range of the x-axis is close to the observed

643   minimum and maximum values in Case 2 (Table S4). The color scale bar represents the pH values.

644   The relative standard deviation (RSD) and range (Range) represent the sensitivity degree of pH to

645   this variable and range (min–max) of the re-predicted pH value in the test, respectively. The square

646   plots on the graph represent the average values of each variable observed in Case 2 with standard

647   deviation as an error bar.

648   Fig. 6 Particle pH calculated with fixed meteorological parameters (T = 275.5 K and RH = 60 %)

649   under different combinations of TNH_x and (a) TH_2SO_4 (Fixed TNO_3 = 67.5 μg/m^3) and (b) TNO_3

650   (Fixed TH_2SO_4 = 36.5 μg/m^3). The color scale bar represents the pH values. The markers on the

651   graph represent the average concentrations of TNH_x, TH_2SO_4, and TNO_3 at the five sites during Case

652   2 with standard deviation as error bar.

653   Fig. 7 Particle pH corresponds to increasing TNH_x at the five sites to examine the effects of major

654   indicators of NH_3 (i.e., TNH_x, Required-NH_x, and Excess-NH_x) on aerosol acidity. Particle pH was

655   calculated by using a wide range of TNH_x (25–130 μg/m^3) and average values of other parameters

656   during Case 2 of each site. The concentrations of TNH_x, Required-NH_x, and Excess-NH_x with

657   corresponding pH values are marked by a hollow box, hollow circle, and arrow respectively. The

658   yellow and blue background colors correspond to the NH_x-poor and NH_x-rich, respectively.
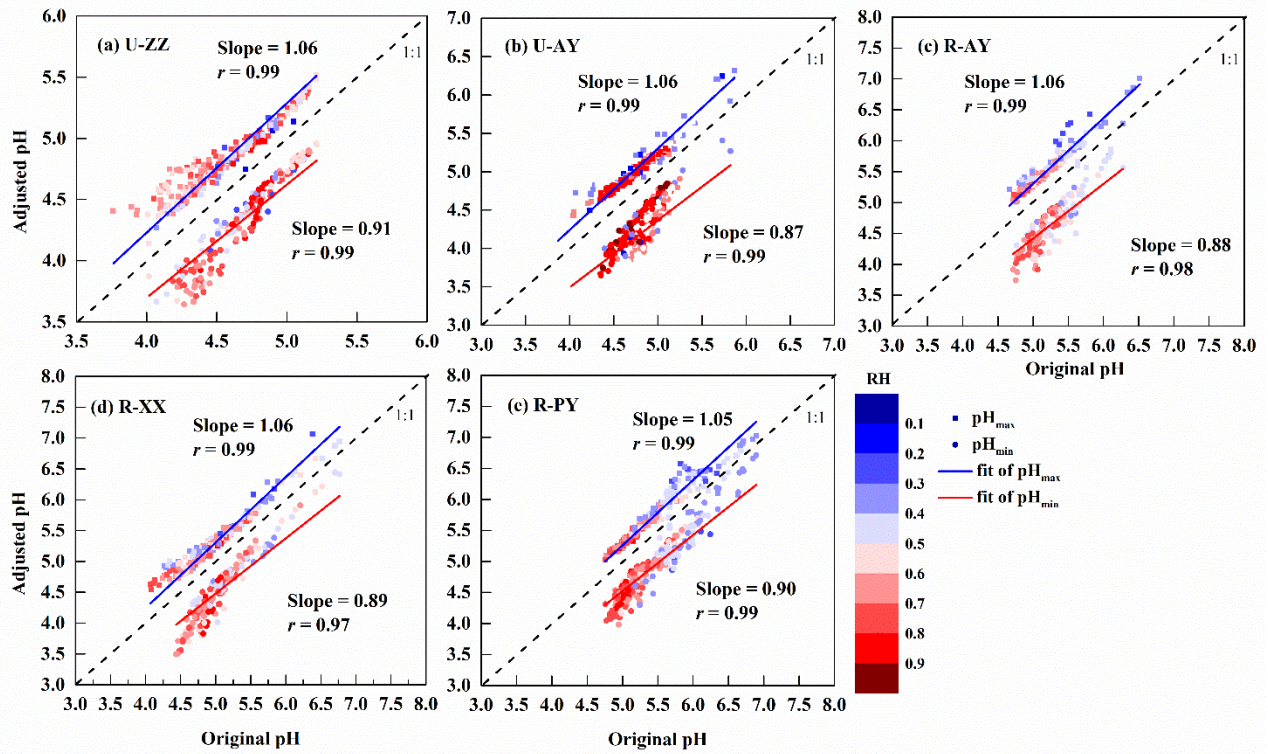
659

660

Fig. 1 pH uncertainties of the five sites based on two extreme scenarios of measurement uncertainty.

Cations and organic carbon concentrations (OC) were adjusted up to within their maximum positive

uncertainties, anions, relative humidity (RH) and temperature (T) were adjusted down within their

maximum negative uncertainties, which represented the pH_{max} case; for pH_{min} case, cations and OC

concentrations were adjusted down, and anions, RH and T were adjusted up. The color scale bar

represents adjusted RH.

668

Fig. 2 Temporal variations of T, RH, wind speed (WS), wind direction (WD), and concentrations of

NH$_3$, NH$_4^+$, SO$_4^{2-}$, and NO$_3^-$ during three cases at the Zhengzhou (U-ZZ) site. The shaded areas

represent the measurement uncertainties.

672

673

674

Fig. 3 Time series and box plot of predicted PM$_{2.5}$ pH, H$^+_{air}$, and aerosol water content (AWC) at the five sites. In each box, the top, middle and bottom lines represent the 75th, 50th, and 25th percentile of statistical data, respectively; the upper and lower whiskers represent the maximum and minimum values, respectively.

681

682   Fig. 4 (a)–(e) Diurnal patterns of median pH values, (f) average RH, and T of the five sites in Case 2.

683   The upper and lower ends of the line represent the maximum and minimum values of pH,

684   respectively. The color scale bar represents AWC concentration.
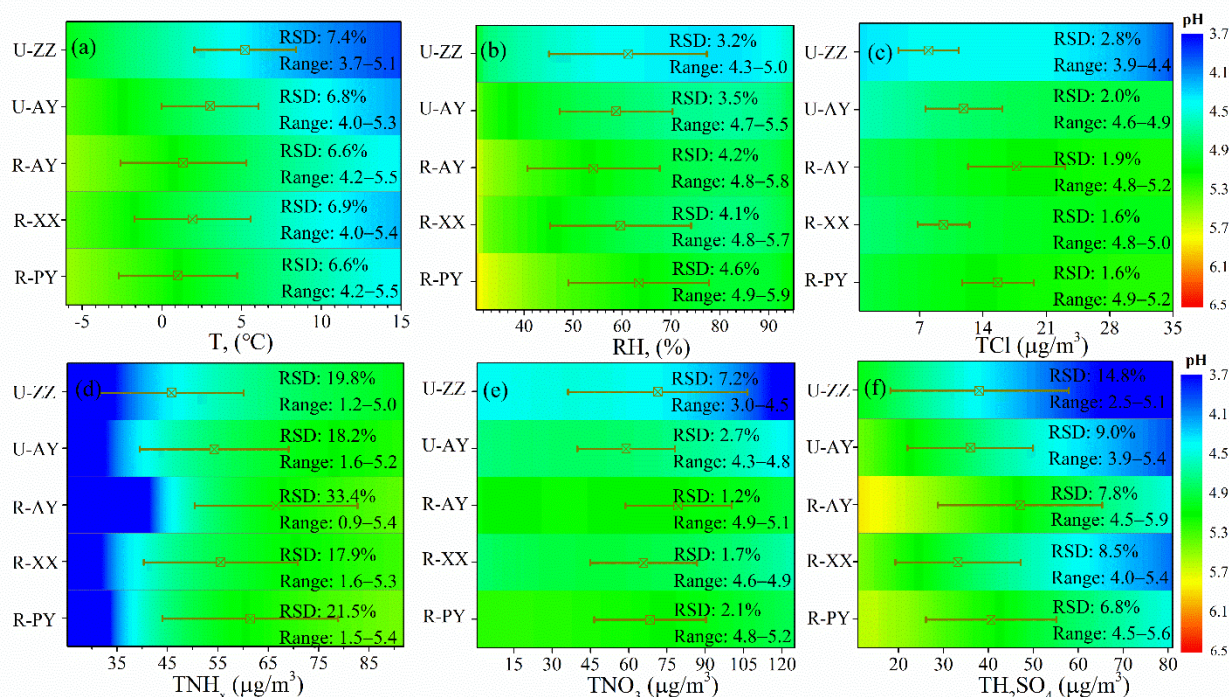
685

686

687

688

Fig. 5 Comparison of the sensitivities of PM$_{2.5}$ pH to T, RH, TCl (HCl$_{(g)}$ + Cl$_{(aq)}^-$), TNH$_x$ (NH$_{3(g)}$ +

NH$_{4(aq)}^+$), TNO$_3$ (HNO$_{3(g)}$ + NO$_{3(aq)}^-$), and TH$_2$SO$_4$ (replaced by observed SO$_4^{2-}$) among the five

sites. A given range for a variable for all sites with corresponding average values of other parameters

was used as input to the ISORROPIA-II model. The range of the x-axis is close to the observed

minimum and maximum values in Case 2 (Table S4). The color scale bar represents the pH values.

The relative standard deviation (RSD) and range (Range) represent the sensitivity degree of pH to

this variable and range (min–max) of the re-predicted pH value in the test, respectively. The square

plots on the graph represent the average values of each variable observed in Case 2 with standard

deviation as an error bar.

702

703
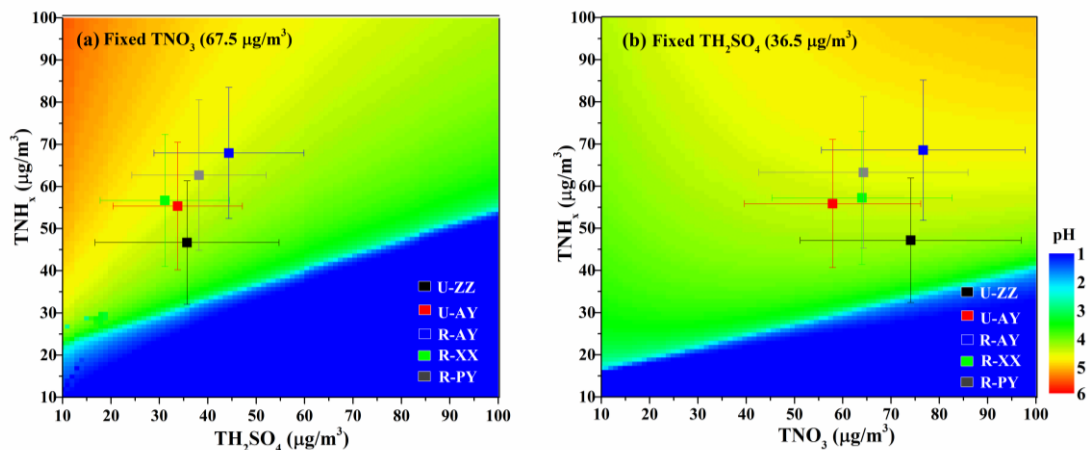
704

705 Fig. 6 Particle pH calculated with fixed meteorological parameters (T = 275.5 K and RH = 60 %)

706 under different combinations of TNH_x and (a) TH_2SO_4 (Fixed TNO_3 = 67.5 µg/m^3) and (b) TNO_3

707 (Fixed TH_2SO_4 = 36.5 µg/m^3). The color scale bar represents the pH values. The markers on the

708 graph represent the average concentrations of TNH_x, TH_2SO_4, and TNO_3 at the five sites during Case
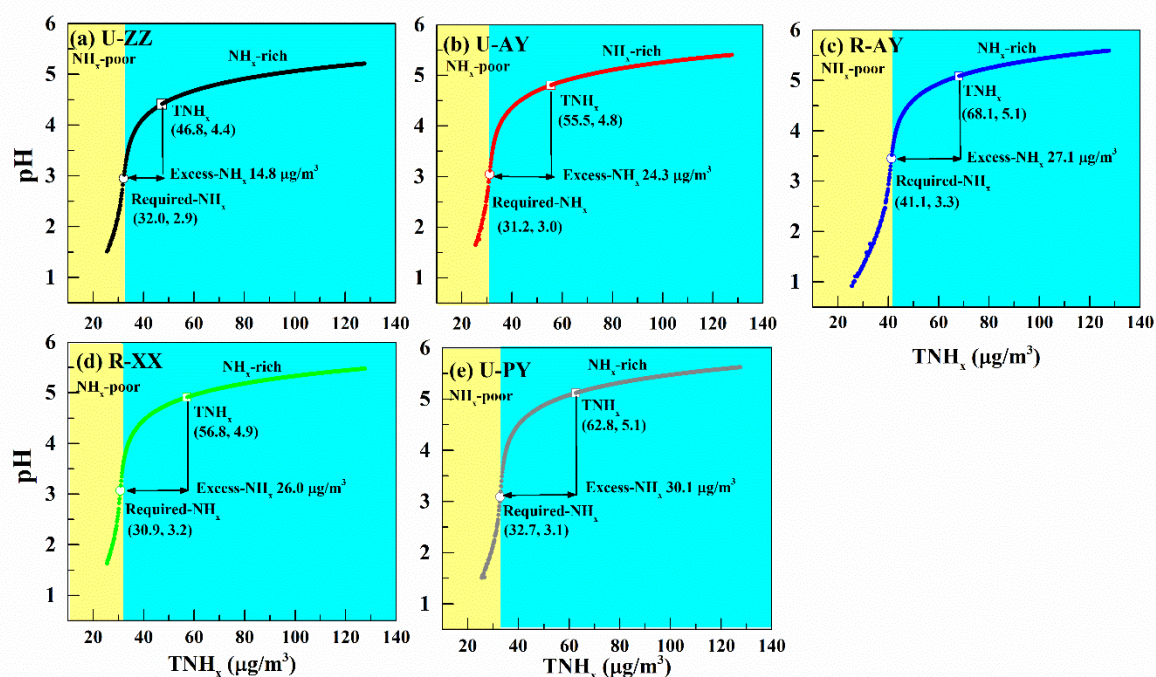
709 2 with standard deviation as error bar.

Fig. 7 Particle pH corresponds to increasing TNH_x at the five sites to examine the effects of major indicators of NH_3 (i.e., TNH_x, Required-NH_x, and Excess-NH_x) on aerosol acidity. Particle pH was calculated by using a wide range of TNH_x (25–130 $\mu g/m^3$) and average values of other parameters during Case 2 of each site. The concentrations of TNH_x, Required-NH_x, and Excess-NH_x with corresponding pH values are marked by a hollow box, hollow circle, and arrow respectively. The yellow and blue background colors correspond to the NH_x-poor and NH_x-rich, respectively.

727

728

729

730

731

732   Table 1 Comparison of the particle pH values in this study (median, min–max) and other sites (mean ± standard deviation).

	Observation site	Period	pH	Model	Reference
This study	Zhengzhou, China (Urban)	Jan 2018	4.5 (3.8–5.2)		
	Anyang, China (Urban)	Jan 2018	4.8 (3.9–5.8)		
	Anyang, China (Rural)	Jan 2018	4.9 (4.1–6.2)	ISORROPIA-II	
	Xinxiang, China (Rural)	Jan 2018	5.1 (4.7–6.3)		
	Puyang, China (Rural)	Jan 2018	5.2 (4.8–6.5)		
China	Beijing, China (Urban)	Feb 2017	4.5 ± 0.7	ISORROPIA-II	Ding et al., 2019
	Beijing, China (Urban)	Dec 2016	4.3 ± 0.4	ISORROPIA-II	Liu et al., 2017
	Beijing, China (Urban)	Jan–Feb 2015	4.5	ISORROPIA-II	Guo et al., 2017
	Xi'an, China (Urban)	Nove–Dec 2012	5.0	ISORROPIA-II	Guo et al., 2017
	Tianjin, China (Urban)	Dec–Jun 2015	4.9 ± 1.4	ISORROPIA-II	Shi et al., 2017
	Tianjin, China (Urban)	Aug 2015	3.4 ± 0.5	ISORROPIA-II	Shi et al., 2019
	Hohhot, China	Winter 2015	5.7	ISORROPIA-II	Wang et al., 2019
	PRD, China (Rural)	Fall-winter season 2012	0.81 ± 0.24	AIM-II model	Fu et al., 2015
	Hong Kong, China (Urban)	2001	0.25	AIM-II model	Pathak et al., 2004
Other countries	Singapore (Urban)	Sep–Nov 2011	0.60	AIM-IV model	Sailesh et al., 2013
	Northeastern US (Urban)	Feb–Mar 2015	0.07 ± 0.96	ISORROPIA-II	Guo et al., 2016
	Alabama, USA (Rural)	Jun–Jul 2013	1.94 ± 0.59	ISORROPIA-II	Guo et al., 2015
	Georgia, USA (Rural)	Aug–Oct 2016	2.2 ± 0.6	ISORROPIA-II	Nah et al., 2018
	Crete, Greece (Background)	Aug–Nov 2012	1.25 ± 1.14	ISORROPIA-II	Boucher et al., 2016

733

734   Table 2 Descriptions of the five sampling sites.

| City | Classification | Site | Coordinate | Location | Surrounding environment | Emission (Gg) | | |
						NH_3[*]	SO_2[**]	NO_x[**]
Zhengzhou	Urban	U-ZZ	34.82° N 113.54° E	West to the Zhengzhou downtown (Zhengzhou University)	Densely occupied residences, light industry, freeways and roads	39.2	36.7	31.8
Anyang	Urban	U-AY	36.09° N 114.41° E	East to the Anyang downtown (Anyang Environmental Protection Bureau)	Occupied residences, heavy industry and traffic roads	57.8	46.9	37.1
	Rural	R-AY	36.22° N 114.39° E	15 km north of Anyang city (Baizhuang town)	High ways, small villages, and cropland			
Xinxiang	Rural	R-XX	35.38° N 114.30° E	35 km northeast of Xinxiang city (Banzao town)	Small villages and cropland	72.1	8.9	19.6
Puyang	Rural	R-PY	36.15° N 115.10° E	44 km north of Puyang city (Liangcun town)	Small villages and cropland	39.6	3.4	3.2

735   [*] Data from a 2015-based NH_3 emission inventory (Wang et al., 2018a).

736   [**] Data from Henan Statistical Yearbook of 2018 (BSH, 2018).

737

738

739

740

741 Table 3 Summary (mean ± standard deviation) of gaseous precursors (μg/m³), water-soluble inorganic ions (μg/m³), T (°C), and RH (%) during three cases

742 of haze periods at five sites.

	Case 1 (January 12−14)					Case 2 (January 14−21)					Case 3 (January 21−25)				
	U-ZZ	U-AY	R-AY	R-XX	R-PY	U-ZZ	U-AY	R-AY	R-XX	R-PY	U-ZZ	U-AY	R-AY	R-XX	R-PY
HNO_3	0.9 ± 0.2	0.7 ± 0.2	3.1 ± 0.2	3.0 ± 0.1	3.9 ± 0.1	1.3 ± 0.3	1.1 ± 0.3	3.7 ± 0.4	3.7 ± 0.5	4.2 ± 0.2	0.9 ± 0.3	0.7 ± 0.2	4.9 ± 1.0	3.3 ± 0.2	3.3 ± 0.2
NH_3	17.0 ± 3.7	19.6 ± 8.0	22.9 ± 6.3	21.6 ± 4.1	17.8 ± 3.7	19.5 ± 5.2	23.6 ± 6.5	25.2 ± 6.5	24.7 ± 9.9	26.5 ± 6.7	10.5 ± 6.9	8.8 ± 4.7	10.6 ± 4.7	8.4 ± 3.5	12.1 ± 3.5
HCl	0.1 ± 0.0	0.7 ± 0.6	0.5 ± 0.1	0.6 ± 0.1	1.8 ± 0.1	0.1 ± 0.1	0.4 ± 0.1	0.6 ± 0.2	0.6 ± 0.1	2.0 ± 0.1	0.1 ± 0.1	0.5 ± 0.1	1.7 ± 0.1	1.0 ± 0.4	1.5 ± 0.4
NO_3^-	41.5 ± 14.6	28.0 ± 14.6	43.0 ± 12.5	32.8 ± 12.9	25.2 ± 9.1	74.2 ± 32.9	58.0 ± 18.3	76.8 ± 21.1	64.1 ± 18.7	64.4 ± 21.7	32.4 ± 13.5	18.9 ± 5.4	26.0 ± 5.8	25.1 ± 6.7	18.8 ± 4.3
NH_4^+	18.6 ± 6.2	15.9 ± 8.3	21.8 ± 8.0	14.9 ± 6.2	12.8 ± 4.5	31.9 ± 12.5	35.2 ± 12.0	47.6 ± 13.1	35.6 ± 10.4	39.9 ± 14.9	17.4 ± 6.0	11.6 ± 4.4	14.3 ± 4.4	12.9 ± 4.0	10.1 ± 2.9
SO_4^{2-}	17.8 ± 7.2	14.4 ± 9.0	13.7 ± 10.0	10.0 ± 5.5	8.6 ± 2.3	38.3 ± 18.0	34.5 ± 13.0	46.8 ± 16.9	32.9 ± 12.5	39.2 ± 13.6	19.8 ± 8.6	15.1 ± 6.1	15.1 ± 7.3	14.4 ± 4.8	13.3 ± 4.0
Ca^{2+}	0.7 ± 0.5	0.5 ± 0.3	5.0 ± 2.2	0.8 ± 0.2	3.4 ± 0.3	0.5 ± 0.4	0.4 ± 0.4	2.2 ± 1.2	1.0 ± 0.3	3.3 ± 0.6	0.1 ± 0.1	0.2 ± 0.2	1.8 ± 0.7	0.5 ± 0.1	2.4 ± 0.5
Na^+	1.5 ± 0.2	1.0 ± 0.0	1.4 ± 0.4	0.7 ± 0.1	2.2 ± 0.1	1.6 ± 0.2	1.0 ± 0.1	1.4 ± 0.4	0.8 ± 0.1	2.2 ± 0.0	1.1 ± 0.2	1.0 ± 0.2	2.2 ± 0.4	1.3 ± 0.4	2.2 ± 0.2
Cl^-	7.5 ± 2.5	2.7 ± 3.4	6.6 ± 2.5	5.4 ± 1.5	6.3 ± 1.2	8.5 ± 3.2	12.0 ± 4.2	18.5 ± 5.0	9.7 ± 2.6	14.4 ± 3.8	3.3 ± 1.5	4.5 ± 1.6	6.9 ± 1.6	4.7 ± 0.9	5.4 ± 1.4
Mg^{2+}	0.2 ± 0.0	0.1 ± 0.0	0.4 ± 0.1	0.1 ± 0.0	0.5 ± 0.0	0.2 ± 0.0	0.1 ± 0.0	0.4 ± 0.4	0.1 ± 0.0	0.5 ± 0.1	0.2 ± 0.0	0.1 ± 0.0	0.4 ± 0.1	0.1 ± 0.1	0.4 ± 0.1
K^+	2.9 ± 0.7	1.4 ± 0.5	1.6 ± 0.6	1.6 ± 0.4	2.5 ± 0.6	4.4 ± 1.7	2.4 ± 0.7	2.9 ± 0.7	1.9 ± 0.6	3.7 ± 1.1	1.9 ± 0.7	0.9 ± 0.3	0.8 ± 0.3	0.8 ± 0.2	1.2 ± 0.4
T	0.3 ± 3.1	−0.9 ± 3.7	−1.8 ± 4.4	−2.0 ± 3.9	−1.7 ± 4.8	4.2 ± 2.2	2.6 ± 2.5	0.1 ± 2.8	1.2 ± 2.9	0.4 ± 3.0	−0.8 ± 1.8	−2.7 ± 1.8	−3.2 ± 1.9	−2.8 ± 2.6	−4 ± 2.3
RH	63.7 ± 12.1	60.3 ± 15.4	54.0 ± 16.0	58.5 ± 13.5	49.7 ± 14.5	66.0 ± 11.4	60.1 ± 9.9	58.6 ± 9.9	62.7 ± 11.6	65.8 ± 11.7	67 ± 13.1	63.7 ± 13.8	55.9 ± 13.6	59 ± 13.7	56.8 ± 16

743

744

745 Table 4 Sensitivity of pH to input data. The real-time measured values of a variable and the average values of other parameters during Case 2 were input

746 into the ISORROPIA II. The degree of sensitivity was represented as the relative standard deviation (%RSD) of the re-calculated pH values, higher RSD

747 implied higher sensitivity of this factor to pH and thus is more important for local pH.

	TH_2SO_4	TNH_x	TNO_3	TNa	TCl	Ca^{2+}	K^+	Mg^{2+}	RH	T
U-ZZ	12.1 %	12.8 %	6.1 %	0.1 %	0.3 %	3.3 %	0.3 %	0.2 %	1.3 %	2.7 %
U-AY	5.8 %	7.4 %	1.0 %	0.1 %	1.1 %	0.4 %	0.3 %	0.0 %	1.6 %	2.8 %
R-AY	6.5 %	10.9 %	1.4 %	0.1 %	0.7 %	1.2 %	0.2 %	0.3 %	1.9 %	2.7 %
R-XX	5.4 %	11.1 %	1.1 %	0.1 %	0.7 %	0.4 %	0.2 %	0.1 %	2.0 %	2.9 %
R-PY	4.7 %	9.4 %	1.5 %	0.0 %	0.7 %	0.5 %	0.4 %	0.1 %	2.3 %	3.1 %

748